Cell Host & Microbe
Article

Anatomically Restricted Synergistic Antiviral Activities of Innate and Adaptive Immune Cells in the Skin

Heather D. Hickman,[1] Glennys V. Reynoso,[1] Barbara F. Ngudiankama,[1] Erica J. Rubin,[1] Javier G. Magadán,[1] Stephanie S. Cush,[1] James Gibbs,[1] Barbara Molon,[2] Vincenzo Bronte,[3] Jack R. Bennink,[1] and Jonathan W. Yewdell[1,*]
[1]Laboratory of Viral Diseases, National Institutes of Allergy and Infectious Diseases, National Institutes of Health, Bethesda, MD 20892, USA
[2]Istituto Oncologico Veneto, Istituto di Ricovero e Cura a Carattere Scientifico (IRCCS), 35128 Padua, Italy
[3]Department of Pathology, Section of Immunology, Verona University Hospital, 37134 Verona, Italy
*Correspondence: jyewdell@mail.nih.gov
http://dx.doi.org/10.1016/j.chom.2013.01.004

SUMMARY

Despite extensive ex vivo investigation, the spatiotemporal organization of immune cells interacting with virus-infected cells in tissues remains uncertain. To address this, we used intravital multiphoton microscopy to visualize immune cell interactions with virus-infected cells following epicutaneous vaccinia virus (VV) infection of mice. VV infects keratinocytes in epidermal foci and numerous migratory dermal inflammatory monocytes that outlie the foci. We observed Ly6G$^+$ innate immune cells infiltrating and controlling foci, while CD8$^+$ T cells remained on the periphery killing infected monocytes. Most antigen-specific CD8$^+$ T cells in the skin did not interact with virus-infected cells. Blocking the generation of reactive nitrogen species relocated CD8$^+$ T cells into foci, modestly reducing viral titers. Depletion of Ly6G$^+$ and CD8$^+$ cells dramatically increased viral titers, consistent with their synergistic but spatially segregated viral clearance activities. These findings highlight previously unappreciated differences in the anatomic specialization of antiviral immune cell subsets.

INTRODUCTION

Skin presents a formidable barrier to pathogen invasion, and many viruses require a breach in the epithelium to establish infection. Some orthopoxviruses, including vaccinia virus (VV), circumvent this problem by infecting epidermal keratinocytes (Moss, 2001), a feature which Jenner famously exploited by epicutaneously infecting patients. Inoculation of virtually the entire human population with VV resulted in the eradication of smallpox, by many measures the most dangerous of all human pathogens (Fenner et al., 1988). While many factors contributed to smallpox eradication, epicutaneous inoculation induces a unique immune response poorly matched by other routes (Liu et al., 2010). Indeed, skin scarification is essential for the generation of tissue-resident memory CD8$^+$ T cells that protect against subsequent poxvirus infection (Jiang et al., 2012).

Due to intense interest in poxviruses as a standard for successful vaccines, a vector for new vaccines (Sutter and Moss, 1992), or potential bioterrorism agents (Lane et al., 2001), the CD8$^+$ T cell response to VV has been remarkably well characterized. VV peptides recognized by human or mouse CD8$^+$ T cells have been identified (Moutaftsi et al., 2006; Tscharke et al., 2005, 2006), leading to definition of robust immunodominance hierarchies of CD8$^+$ T cells responding to individual viral peptides (Flesch et al., 2010; Tscharke et al., 2005, 2006; Yewdell, 2006). Knockout mice have revealed gene products governing the strength of the VV-specific CD8$^+$ T cell response (Remakus and Sigal, 2011; Salek-Ardakani et al., 2009; Seedhom et al., 2012; Zhao and Croft, 2012).

Despite numerous ex vivo studies, surprisingly little is known about the stoichiometric and spatiotemporal organization of individual T cells interacting with virus-infected cells in situ. Detailed understanding has, in part, been hampered by difficulty visualizing viral infection during the course of a natural replicative cycle in vivo. Though live recombinant VV (rVV) and vesicular stomatitis virus (VSV) have been visualized in lymph nodes (LNs) draining subcutaneous injection sites (Hickman et al., 2011, 2008; Iannacone et al., 2010), neither virus replicates extensively nodally (Hersperger et al., 2012; Simon et al., 2007). Additionally, rVV- and VSV-infected LN cells die due to viral cytopathic effects before naive T cells achieve full effector functions, precluding their study as CD8$^+$ T cell targets (Hickman et al., 2008). Thus, a critical unresolved question is how CD8$^+$ T cells physically eliminate virus-infected cells and ultimately control active sites of viral replication in situ.

In the present study, we use both static ex vivo and dynamic intravital multiphoton microscopic (MPM) imaging to better understand CD8$^+$ T cell-mediated control of virus replicating in the skin. We found unexpected spatial organization and trafficking of effector CD8$^+$ T cells. Rather than target infected keratinocytes, CD8$^+$ T cells pursue and lyse infected inflammatory monocytes that outlie lesions. In a sophisticated orchestration of immune cell subsets, optimal virus clearance is achieved by coordination of physically partitioned CD8$^+$ cells and Ly6G$^+$ innate immune cells.

RESULTS

Visualization of Epicutaneous Vaccinia Virus Infection

To image rVV skin infection, we infected B6 mice epicutaneously in the ear pinna with the bifurcated needle routinely used for

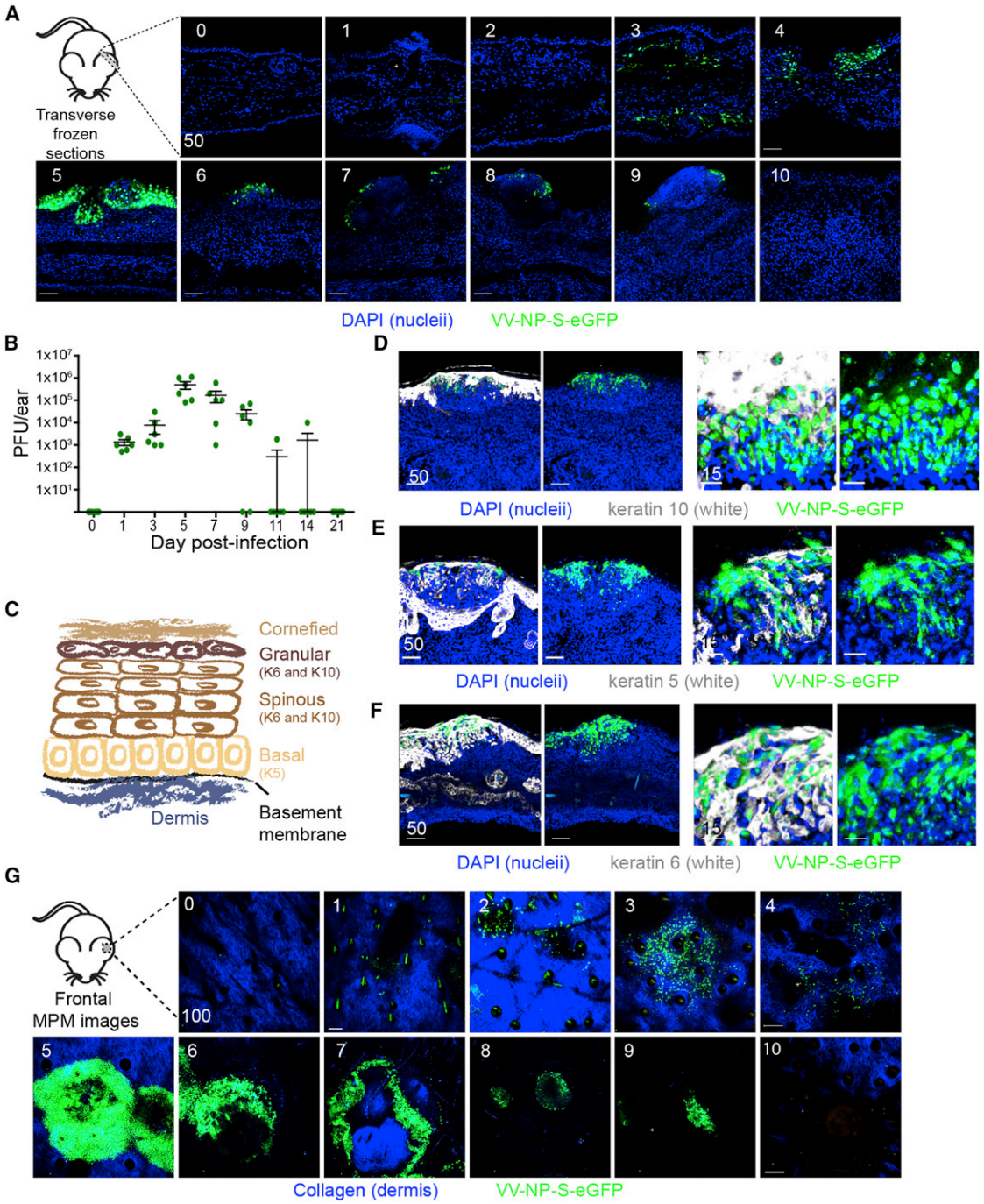

Figure 1. Imaging Vaccinia Virus Infection of the Skin

(A) Confocal images of transverse ear sections. Upper left corner of each frame = d.p.i. Blue (DAPI) = nuclei; green = virus-infected cell.

(B) Viral titer/ear determined by plaque assay at indicated d.p.i. Dots represent individual ears. Error bars = SEM.

(C) Schematic of skin and representative keratins.

(D–F) Confocal images of transverse ear sections taken 5 d.p.i. Keratin 10 (D), 5 (E) or 6 (F) staining = white, nuclei = blue (DAPI), virus-infected cells = green. Higher magnification views shown in the two panels on the right; white staining is omitted.

(G) MIPs of MPM images of frontal ear sections. Dermis = blue (SHG), virus-infected cell = green. Scale bars = μm.

human smallpox vaccination. To optimize the sensitivity and precision of infected cell tracking, we used an rVV expressing an eGFP (enhanced green fluorescent protein) fusion protein targeted to the nucleus of infected cells (VV-NP-S-eGFP) (Hickman et al., 2011, 2008; Norbury et al., 2002). In frozen transverse sections of infected ears (Figure 1A), we detected small numbers

of isolated eGFP$^+$ cells as early as 3 days postinfection (d.p.i.) By plaque assay, infected cell numbers peaked at 5 d.p.i., a time when a majority of infected cells were physically located in large epidermal keratinocytic foci (Figures 1A and 1B).

To determine the precise location of rVV-infected cells in epidermal foci, we stained for keratins present in different layers of the epidermis (illustrated in Figure 1C; reviewed in Freedberg et al., 2001). Staining with keratin 10 localized infection to the suprabasal layers of the epidermis (Figure 1D), which was confirmed by location and lack of staining with the basal cell marker keratin 5 (Figure 1E). rVV infection induced keratin 6 expression (Figure 1F), which is synthesized by hyperproliferative keratinocytes during wound healing (Navarro et al., 1995; Weiss et al., 1984).

We next examined epicutaneously infected ears using MPM (Figure 1G), distinguishing the dermis by collagen expression (detected via second harmonic excitation [Li et al., 2012]). Paralleling plaque assays, eGFP$^+$-infected cells were detected in the dermis at 1 d.p.i. and accumulated in number before the appearance of the large keratinocytic foci. By 10 d.p.i., we no longer detected infected cells in most mice. Thus, MPM detects epicutaneous rVV infection of both dermal cells and epidermal keratinocytes.

Migratory Inflammatory Macrophages Are Infected by VV

Though MPM imaging studies have yet to report mobile virus-infected cells (Hickman et al., 2011, 2008; Iannacone et al., 2010; Junt et al., 2007), migratory cells likely play important roles in initiating antiviral responses (Bedoui et al., 2009). MPM imaging over short time periods (30 min to 2 hr) revealed many motile eGFP$^+$ dermal cells (Figure 2A and Movie S1). Flow cytometry of cells isolated from ears 5 d.p.i. revealed numerous infected (eGFP$^+$) CD45$^+$ leukocytes, a majority of which (~75%) were CD11b$^+$ GR-1^{int} inflammatory monocytes (fully characterized as CD45$^+$ CD11b$^+$ GR-1^{int} LY6G$^-$ F4/80$^-$ CD11c$^-$ cells [Figure 2B]). Inflammatory monocytes represent the prevalent infected skin leukocyte over the infection course peaking 4–5 d.p.i. before greatly decreasing in number on day 6 (Figure 2C). Notably, we also identified minor populations of eGFP$^+$ dendritic cells (DCs) and Ly6G$^+$ cells (neutrophils and recently defined Ly6G$^+$ monocytes [Fischer et al., 2011]) (Figures 2C and S1).

Via MPM, many of the infected dermal cells appeared just outside major keratinocytic foci. Immunohistology of frozen sections revealed that outlying infected cells expressed CD11b (Figure 2D), consistent with a macrophage lineage. As expected, MPM imaging revealed that infected cells in large epidermal keratinocytic foci were essentially sessile, with average speeds < 1 μm/min (Figures 2E and 2F and Movie S1). Many infected cells outside of major lesions were motile, however, with an overall average speed of >2 μm/min (Figure 2F). Motile infected cells (defined as cells with average speeds > 4 SD from cells in foci) exhibited average speeds of ~4 μm/min, similar to a moderately motile lymph node cell (Lindquist et al., 2004).

To further examine the mobility of infected inflammatory monocytes, we imaged LysM-eGFP mice (with green myelomonocytes [monocytes, macrophages, and neutrophils] [Faust et al., 2000]) infected with an rVV expressing blue fluorescent protein VV-BFP-Ub-S (VV-BFP-ubiquitin-SIINFEKL, as described in Lev et al., 2010, pseudocolored magenta) (Figure 2G and Movie S1). This revealed many motile eGFP$^+$ cells (myelomonocytes) that were also BFP$^+$ (infected with rVV).

To determine if these cells were productively infected (able to generate infectious virus progeny), we sorted CD45$^+$ eGFP$^+$ cells from collagenase-digested ears 5 d.p.i. and performed plaque assays (Figures 2H–2J). At peak infection, we estimated 3 × 10^5 infected inflammatory monocytes per ear, from which we recovered 6.5 × 10^4 plaque-forming units (pfu) of virus (Figure 2I). In contrast, virus was not recovered from eGFP$^-$ CD45$^+$ cells from the same ears. Comparison to virus isolated from the total cell population (including keratinocytes) before sorting revealed that inflammatory monocyte-produced virus accounted for ~7% of the virus recovered 5 d.p.i. (Figure 2J). Together, these data indicate that VV productively infects numerous GR-1^{int} inflammatory monocytes that surround keratinocytic foci and that these highly motile cells produce infectious virus.

Uninfected Inflammatory Monocytes Rapidly Respond to rVV Infection

Skin injury or infection induces migration of circulating blood neutrophils, monocytes, and eventually lymphocytes to the inflammation site (Werner and Grose, 2003). Flow cytometry of dissociated ears revealed that most infiltrating cells were inflammatory monocytes (Figure 3A). Based on expression of the rVV reporter gene, most inflammatory monocytes in the skin were uninfected with approximately 10% peak eGFP expression at 3 d.p.i. (Figure 3B). Immunohistology of frozen sections revealed elevated numbers of CD11b$^+$ cells adjacent to infected cells, penetrating dense infected keratinocytic foci 5 d.p.i. (Figure 3C).

We again used LysM-eGFP mice (eGFP$^+$ myelomonocytes) infected with a BFP-expressing rVV (VV-NP-S-BFP, pseudocolored magenta) to identify rVV-infected cells by MPM (Figure 3D). High numbers of motile, uninfected eGFP$^+$ cells accumulated at the infection site rapidly postinfection (Movie S2). By 4–5 d.p.i., uninfected eGFP$^+$ cells had invaded viral foci (Figures 3D and 3E). Immunohistology showed that foci-infiltrating cells expressed both GR-1 and Ly6G (Figure 3F), indicating that these cells were not canonical GR-1^{int} LY6G$^-$ inflammatory monocytes, but rather either Ly6G$^+$ monocytes (Fischer et al., 2011) or neutrophils. While their late appearance and slower motility than typical neutrophils (Chtanova et al., 2008) would be consistent with LY6G$^+$ monocytes, caution dictates that we refer to them henceforth as Ly6G$^+$ cells. Treatment of mice with a depleting anti-Ly6G antibody resulted in lesions devoid of eGFP$^+$ cellular infiltration, yet clearly spared many outlying eGFP$^+$ cells (Figure 3G). Thus, both inflammatory monocytes and Ly6G$^+$ cells respond vigorously to epicutaneous infection, with Ly6G$^+$ cells penetrating epidermal foci.

What is the function of infiltrating cells during rVV infection? Both monocytes and neutrophils can produce reactive oxygen and nitrogen species (ROS and RNS, respectively) at sites of inflammation (Babior, 2004; Halliwell, 2006). To determine which infiltrating cells produced ROS, we isolated cells 5 d.p.i. and treated them with a cell-permeant substrate (CellROX) that becomes fluorescent upon oxidation (Figure 3H). Both inflammatory monocytes and Ly6G$^+$ cells produced ROS, with the highest fluorescence observed in the latter. ROS and RNS can induce cellular, DNA, and protein damage through production of

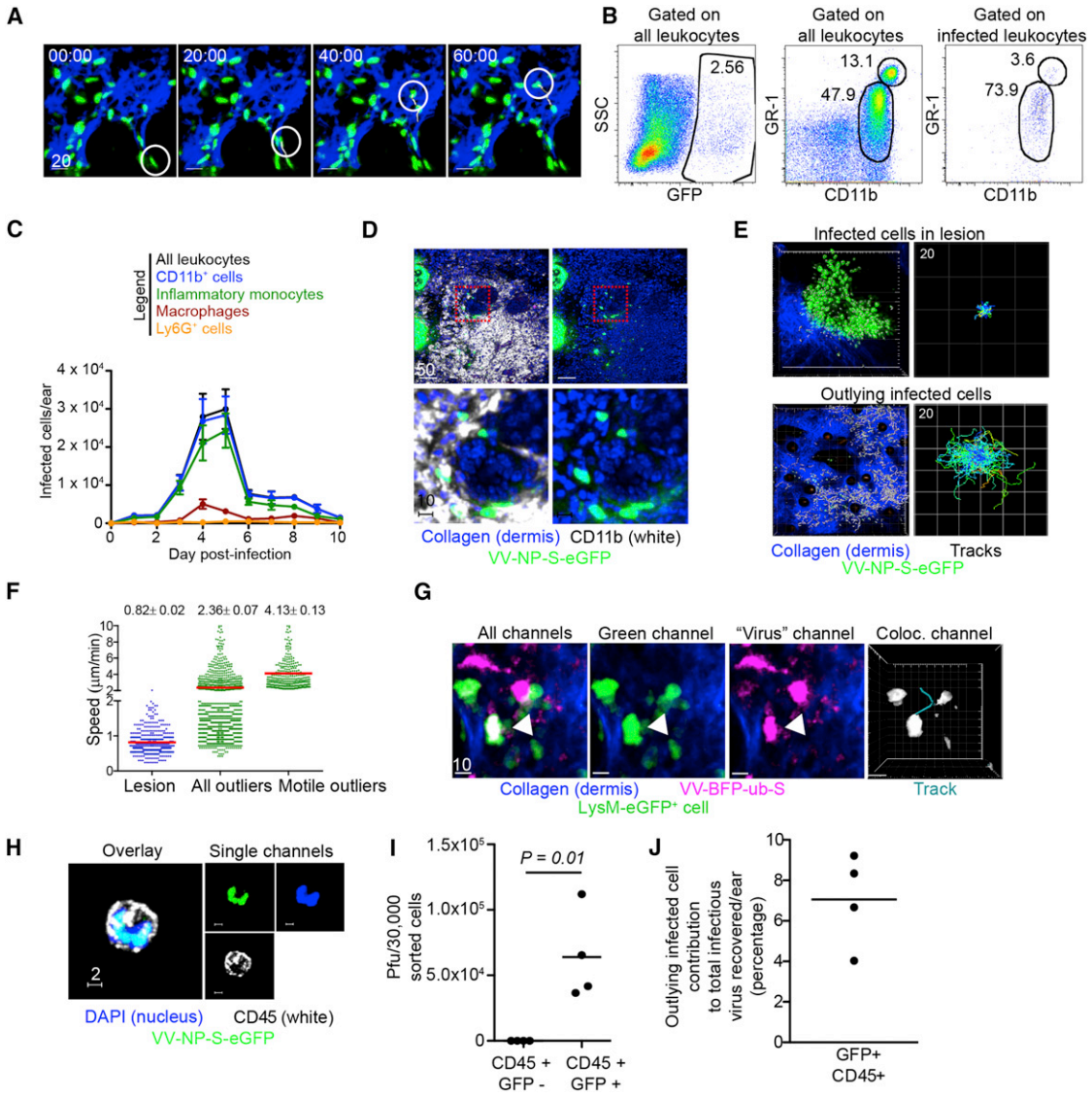

Figure 2. Mobile Inflammatory Monocytes that Outlie Keratinocytic Lesions Are Infected

(A) MPM images of mobile infected cells in the dermis. Virus-infected cell = green, dermis = blue, time = min. A highly motile cell is circled; track shown in white.

(B) Representative flow dot plots of cells recovered from collagenase-dissociated ears at 5 d.p.i. Plots were gated on CD45$^+$ leukocytes. Middle panel shows total CD11c$^-$, CD11b$^+$, GR-1^{int}, and ^{hi} cells. Right panel gated only on infected (eGFP$^+$) cells.

(C) Number of each subset of infected cells per ear. N = 6 ears/time point. Error bars = SEM.

(D) Confocal images of frontal ear sections at 5 d.p.i. with VV-NP-S-eGFP (virus = green, nuclei = blue (DAPI), CD11b staining = white). Bottom panels: higher magnification of red dashed boxes. Right panels: no white staining.

(E) MPM images of infected cells in a keratinocytic lesion at 5 d.p.i. (top panels) or in outlying cells (bottom panels) over a 2 hr period. Virus-infected cells = green, dermis = blue. Right panels: Cell migration tracks of infected cells translated to the same origin. Scale is shown in upper left in μm/box of grid (note that grid area is larger for outlying infected cells [bottom]). Tracks classified by mean cell speed (slow [blue] to fast [red]).

(F) Mean cellular speed within lesion (blue dots), outside of lesion (green dots), or those >4 SD from speeds of those in lesion (green dots, right). Average speeds and SEM shown.

(G) MPM images of a LysM-eGFP mouse infected with VV-BFP-Ub-S (pseudocolored magenta). Colocation of green/magenta is shown in white. Cell migration track (right panel). Scale bars = μm.

(H) Confocal image of a sorted eGFP$^+$ CD45$^+$ cell as overlay (left panel) or individual channels (right panels). CD45 = white, VV-NP-S-eGFP = green, nuclei = blue.

(I) Viral titers from sorted, infected (eGFP$^+$), or uninfected (eGFP$^-$) CD45$^+$ cells at 5 d.p.i., normalized to the average number of infected cells recovered per ear.

(J) Contribution of outlying infected cells to total infectious virus at 5 d.p.i. Each experiment was repeated 3–4 times with three to ten mice per group. Scale bars = μm. See also Figure S1 and Movie S1.

peroxynitrite, a powerful oxidizing and nitrating agent typically detected by the presence of nitrotyrosine (Szabó et al., 2007). Immunohistology of LysM-eGFP$^+$ mice infected with VV-NP-S-BFP with anti-nitrotyrosine antibody revealed intense staining in and around foci in areas dense with infiltrating eGFP$^+$ cells (myelomonocytes) (Figure 3J). Importantly, nitrotyrosine staining

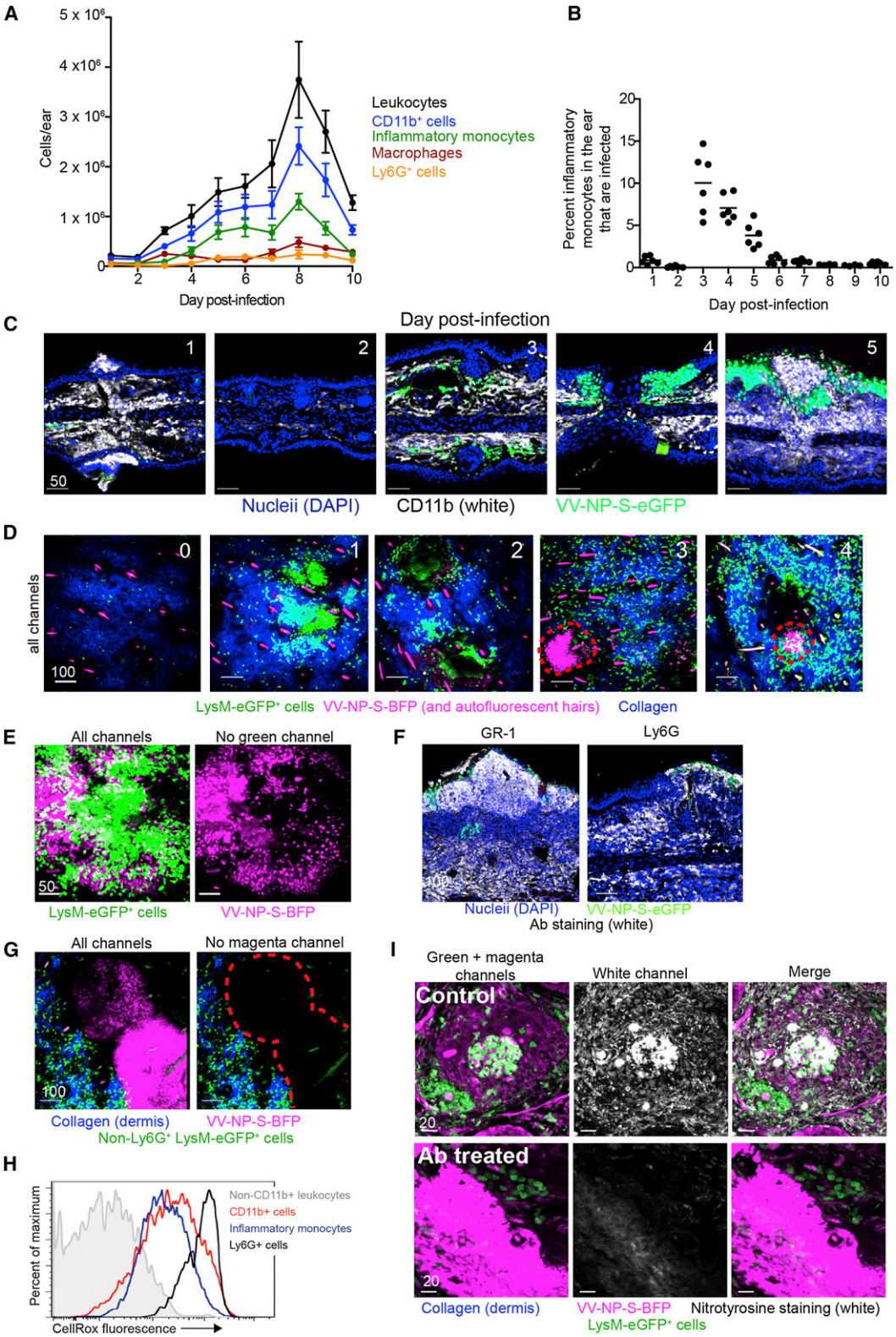

Figure 3. Innate Cells Immigrate into Tissue and Infiltrate Keratinocytic Lesions

(A) Number of cells per subset per d.p.i. N = 6 ears/time point. Error bars = SEM.

(B) Percent of total CD11b$^+$ GR-1^{int} Ly6G$^-$ F4/80$^-$ CD11c$^-$ cells infected with VV (expressing eGFP) at each d.p.i. Line = mean. Dots = individual ears.

(C) Confocal images of transverse ear sections. CD11b = white, nucleii = blue, virus-infected cell = green, d.p.i. in upper right corner.

(legend continued on next page)

was eliminated by depletion of GR-1$^+$ (Ly6CG$^+$) cells even in heavily infected areas (Figure 3I). Taken together, these data strongly suggest that infiltrating inflammatory monocytes and Ly6G$^+$ cells produce ROS that eventually lead to protein nitration in and around viral lesions.

CD8$^+$ T Cells Eliminate Infected Inflammatory Monocytes

CD8$^+$ T cells participate in controlling VV infection after either intraperitoneal (i.p.) or intranasal (i.n.) infection (Moutaftsi et al., 2009; Xu et al., 2004), and long-lasting immunity generated by VV vaccination is CD8$^+$ based (Liu et al., 2010). Therefore, we originally hypothesized that antigen-specific CD8$^+$ T cells would enter keratinocytic lesions and eliminate infected cells.

We analyzed effector CD8$^+$ T cell behavior by adoptively transferring 2 × 10^5 dsRed OT-I TCR transgenic CD8$^+$ T cells (which recognize K^b-SIINFEKL), infecting, and performing flow cytometry on dissociated ears. OT-I cells appeared 5 d.p.i., plateaued in number at 6–7 d.p.i., and decreased at 8 d.p.i. (Figure 4A). Surprisingly, MPM revealed that mobile T cells encircled, but did not penetrate, keratinocytic foci, instead moving in paths just outside of the lesions (Figures 4B and 4C). Side views of 3D reconstructions of either MPM or cryosection z-slices revealed that T cells were located in the dermis (blue) surrounding and beneath epidermal lesions at 5–6 d.p.i. (Figures 4D and 4E and Movie S3). By 7 d.p.i. most lesions appeared "open" (with a nonfluorescent center) with small numbers of T cells penetrating (Figure 4D, bottom panel). We confirmed the spatial separation of T cells and lesions by transferring dsRed OT-I cells into LysM-eGFP mice and infecting with NP-S-BFP (Figure S2 and Movie S3). Taken together, these data indicate that CD8$^+$ T cells infrequently infiltrate large keratinocytic foci, consistent with the idea that CD8$^+$ T cells play only a limited role in clearing virus from these lesions.

Could CD8$^+$ T cells be patrolling the lesion periphery to deal with outlying cells infected by virus emanating from the lesion? MPM revealed that CD8$^+$ T cells actively pursued outlying infected inflammatory monocytes, often extending pseudopodia through tight spaces to contact infected cells (Figure 4E). In several instances, we imaged CD8$^+$ T cells killing outlying infected cells, generating eGFP-containing cell debris, and then retreating (Figures 4F and 4G and Movie S3). Using a spot detection algorithm to further characterize fragments in one instance, a single GFP$^+$ cell broke into >6 spots with diminishing diameter and fluorescence (Figure 4H). After substantial numbers of T cells had entered the skin, most of the eGFP signal near large foci was restricted to cell fragments <5 μm in diameter (compared to 10–15 μm for intact cells), consistent with efficient CD8$^+$ T cell-mediated destruction of virus-infected outlying cells (Movie S3).

To quantitate the participation of CD8$^+$ T cells in eliminating rVV-infected cells outside foci, we enumerated infected cells at different d.p.i. (Figure 4I). As before, gating on CD45$^+$ cells (those of hematopoietic origin) revealed that ~2% of the total leukocytes in the ear were rVV-infected 5 d.p.i. When high numbers of OT-I cells were present in the skin 6 d.p.i., we no longer detected large quantities of eGFP$^+$ infected cells. CD8$^+$ depletion increased numbers of infected cells, while NK depletion had a minor effect (Figure 4J). Under the same conditions, infection with rVV lacking OT-I cognate Ag (VV-NP-eGFP) increased infected cell numbers relative to infection with VV-NP-S-eGFP (Figure 4K). This effect was less dramatic, however, than total CD8 depletion, demonstrating a role for endogenous CD8$^+$ T cells in clearing infected leukocytes but also showing that endogenous responders are limiting at this time point.

Taken together, these data indicate that CD8$^+$ T cells are principally responsible for elimination of infected inflammatory monocytes that outlie major keratinocytic foci.

Chemokines Are Induced by VV Scarification and Localize to Viral Lesions

How are CD8$^+$ T cells physically excluded from lesions, while Ly6G$^+$ cells readily enter? Molon et al. (2011) described a similar phenomenon in antitumor responses due to chemokine nitration. While monocytes responded to nitrated chemokines and entered tumors, T cells could not. To determine if a similar mechanism occurred after rVV infection, we quantitated temporal chemokine production in the ear using multiplex protein analysis (Figure 5A). CCL2, a monocyte chemoattractant (reviewed in Deshmane et al., 2009), exhibited the largest early increase, consistent with the rapid response of inflammatory monocytes. Levels of T cell-tropic CCR5-ligand chemokines CCL3, CCL4, and CCL5 increased beginning 5 d.p.i., concomitant with T cell entry into the ear. Since we previously reported that CCR5-ligand chemokine expression attracts OT-I CD8$^+$ T cells and partially dictates their location after lymph node rVV infection (Hickman et al., 2011), we next determined chemokine location in the infected skin. Immunohistology of LysM-eGFP$^+$ ears 5 d.p.i. with VV-NP-S-BFP (Figure 5B) revealed both CCL3 and CCL5 (and less intense CCL4) staining concentrated in and around rVV lesions. Thus, T cell-tropic chemokines are produced after rVV infection and found within viral lesions, but T cells do not enter the lesion.

The presence of eGFP$^+$ myelomonocytes producing ROS in the same area as the heaviest chemokine staining suggested possible protein nitration. Thus, we stained sections 5 d.p.i. for both nitrotyrosine (red) and CCL3 (gray) (Figure 5C). The two stains colocalized intensely inside the lesion and outside lesions to a lesser extent. Calculating the ratio of CCL3 (the CCR5-ligand

(D) MIPs of MPM images (frontal sections) of LysM-eGFP mice (green macrophages, monocytes, and neutrophils) infected with VV-NP-S-BFP (pseudocolored magenta). Dermis = blue, red dashed lines highlight lesions, d.p.i. in upper right corner.
(E) Higher magnification images of LysM-eGFP at 5 d.p.i. Right panel: only infected cells (magenta).
(F) Transverse ear section at 5 d.p.i. with NP-S-eGFP (green), stained for with GR-1 (Ly6CG, left) or LY6G (right). Staining = white, nuclei = blue (DAPI).
(G) MIP of MPM images of LysM-eGFP mice at 5 d.p.i. with VV-NP-S-BFP (pseudocolored magenta) after anti-Ly6G antibody depletion.
(H) Flow cytometric histograms showing CellROX fluorescence (ROS indicator) by each cell subset.
(I) Frozen sections from LysM-eGFP mice at 5 d.p.i. with VV-NP-S-BFP (pseudocolored magenta) stained for nitrotyrosine (white). Top panels: control mice. Bottom panels: anti-Ly6CG-depleted mice. White channel alone (middle). Confocal images were repeated twice. Other experiments were repeated 3–4 times with three to four mice per group. Scale bars = μm. See also Movie S2.

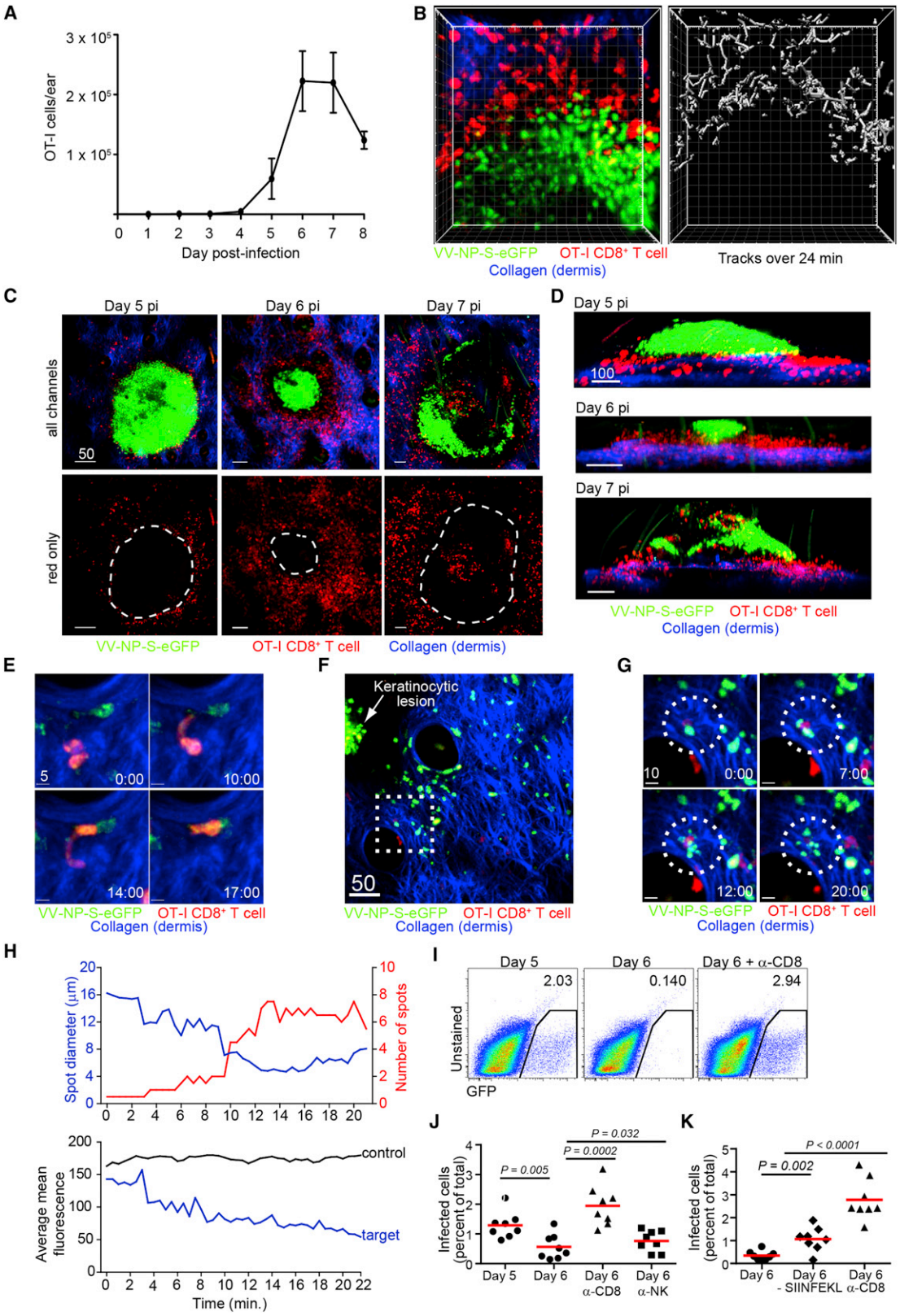

Figure 4. CD8⁺ T Cells Are Excluded from Lesions but Eliminate Peripheral Infected Inflammatory Monocytes

(A) OT-I CD8⁺ T cells in ear after VV-NP-S-eGFP infection. A total of 2 × 10^5 dsRed OT-I CD8⁺ T cells were adoptively transferred prior to infection. Error bars = SEM; N = 8 ears/d.p.i.

(legend continued on next page)

chemokine with the best immunohistochemical staining) to nitrotyrosine staining revealed that the ratio of CCL3/nitrotyrosine was much higher outside lesions than within (Figures 5D–5G). To quantify this effect, we analyzed ~25 higher magnification images, categorized as either lesion-bearing (Figure 5E) or outlying infected cell-bearing (Figure 5F), and calculated the CCL3/nitrotyrosine ratio (Figure 5G). We found a CCL3/nitrotyrosine ratio of 1.06 inside lesions versus 1.95 outside in areas containing infected inflammatory monocytes.

Thus, although nitrotyrosine was present in both areas, unmodified chemokine is favored outside viral lesions. Taken together, these data are consistent with chemokine nitration controlling T cell localization within and around VV lesions.

Peroxynitrite Products Dictate T Cell Location during Infection

If chemokine nitration (or nitration of any chemoattractant) dictates T cell exclusion from lesions, inhibition of peroxynitrite could result in T cell penetration. To test this, we transferred dsRed OT-I cells into LysM-eGFP mice and infected with VV-NP-S-BFP. At 4 d.p.i. we treated with a single dose of (3-[aminocarbonyl]furoxan-4-yl)methyl salicylate (AT38), a potent inhibitor of peroxynitrite generation (Molon et al., 2011). Remarkably, MPM images of AT38-treated mice showed a clear redistribution of T cells into viral lesions (Figure 6A, top panels, and Movie S4). Although lesion size at 5 d.p.i. was unaffected by AT38 treatment (Figure S3), the number of $CD8^+$ T cells within lesion boundaries increased ~3.5-fold (Figure 6B).

Presumably, relocated T cells could now eliminate previously inaccessible virus-infected keratinocytes. In this case we would predict that lesions would no longer appear as solid spheres of fluorescence, but instead have dark regions where fluorescent-infected keratinocytes once lurked. Examination of lesion morphology 6 d.p.i. (1 day after initial T cell entry) in the presence or absence of AT38 (Figures 6C and 6D) revealed that lesions in control mice remained largely in a closed conformation (e.g., no dark center). Significantly more lesions in treated mice were open (dark center) and often discontinuous. Importantly, treatment with AT38 in conjunction with $CD8^+$ T cell depletion eliminated lesion opening, demonstrating that $CD8^+$ T cells were required for this effect. Consistent with enhanced $CD8^+$ T cell encounters with virus-infected cells inside the lesion, we observed a trend toward elevated numbers of OT-I production of IFN-γ in AT38-treated mice (Figure 6E).

Next, we visualized $CD8^+$ T cell interactions with infected keratinocytes inside viral lesions after AT38 treatment (Figure 6F). T cells formed long-lasting interactions with keratinocytes, and in several instances we observed retreating T cells containing fluorescent keratinocyte fragments, consistent with killing. Moreover, AT38 treatments decreased virus titers 2-fold at 6 d.p.i., consistent with T cell effector function (Figure 6G). By 7 d.p.i. lesions were naturally opened, and there was no significant difference in AT38- versus vehicle-treated mice (Figure 6G), providing an internal control for the nonspecific effects of AT38 on virus recovery.

Taken together, these data suggest that peroxynitrite products control $CD8^+$ T cell entry into, and consequent activity within, viral lesions.

$CD8^+$ T Cells and $Ly6G^+$ Cells Synergize to Clear Epicutaneously Administered Virus

The locations of $Ly6G^+$ cells within lesions and $CD8^+$ T cells outside lesions suggested specific functions for each cell subset in rVV clearance. As described above, $CD8^+$ T cells eliminate outlying infected inflammatory monocytes (Figure 4). To examine the role of $CD8^+$ T cells in resolving lesions, we infected mice with rVV, allowed effector T cells to eliminate outlying infected cells (which occured prior to 6 d.p.i.), then antibody-depleted $CD8^+$ T cells (Figure 7A). After 4 days, we examined the number and type of lesions in the presence or absence of $CD8^+$ T cells (Figure 7B). Under both conditions we observed a few remaining lesions with hollow, nonfluorescent centers (open) along with many partially resolved lesions (disturbed collagen but no remaining fluorescence). Statistically, CD8 depletion had no effect on the number of open, fluorescent lesions (Figure 7B). Hence, $CD8^+$ T cells are not necessary for viral lesion clearance after the initial elimination of outlying virus-infected inflammatory monocytes.

By contrast, treating mice with anti-Ly6G antibody to deplete lesion-infiltrating $Ly6G^+$ cells delayed clearance of lesions (Figure 7C), with >80% of 7 d.p.i. lesions remaining in a solidly fluorescent, closed conformation, compared to only ~20% in control mice (Figure 7D). However, viral titers were only increased ~3.25-fold by $Ly6G^+$ cellular depletion (Figure 7E). Thus, although $Ly6G^+$ monocytes infiltrate lesions and are more efficient at viral clearance than relocated T cells (Figure 6G), they cannot single-handedly eliminate all infectious virus in the skin.

Since neither $CD8^+$ T cells nor $Ly6G^+$ monocytes alone could control viral infection, we addressed their potential synergism

(B) MIP MPM images of OT-I $CD8^+$ T cells (red) at the border of a keratinocytic focus (green). Dermis = blue. Tracks of T cells over 24 min (right panel). Individual boxes = 10 μm.
(C) MIP MPM images. OT-I $CD8^+$ T cells = red, virus-infected cell = green. Bottom panels: only $CD8^+$ T cells with lesion location outlined (dashed lines).
(D) Side views of MIP MPM images showing T cell (red) location relative to keratinocytic lesion (green).
(E) MIP MPM images of an OT-I cell (red) squeezing through the dermis (collagen; blue) to interact with a VV-NP-S-eGFP-infected cell (green).
(F) MIP MPM image of OT-I $CD8^+$ T cells (red) outside of a keratinocytic lesion (green, indicated with a white arrow). Dashed box shown in higher magnification.
(G) MPM images of a T cell killing a VV-infected cell. Time (min) shown in lower right. Dashed circle highlights interaction.
(H) Spot calculations of target cell. Top panel: number of spots detected (red) compared to the average diameter of spots (blue). Bottom panel: mean fluorescence of all spots (blue) compared to a nontarget control.
(I) Flow cytometric plots of GFP^+ infected cells recovered 5 (left) or 6 (middle) d.p.i. Right: plot at 6 d.p.i. with CD8-depleting antibody throughout infection. Numbers indicate percentage of $eGFP^+$ leukocytes recovered.
(J) Individual ears from mice at 5 d.p.i. (dots, left), 6 d.p.i. (dots, middle left), 6 d.p.i. with anti-CD8 (triangles), or 6 d.p.i. with anti-NK1.1 (squares). Lines show means.
(K) As in (J) but with mice infected with a virus lacking SIINFEKL (middle diamonds and triangles) compared to one expressing cognate antigen for OT-I cells (circles). Flow experiments were performed at least 3 times with 3–5 mice/group. Statistics = Student's t test. MPM imaging experiments were performed at least 6 times with two to five mice per group. Scale bars = μm. See also Figure S2 and Movie S3.

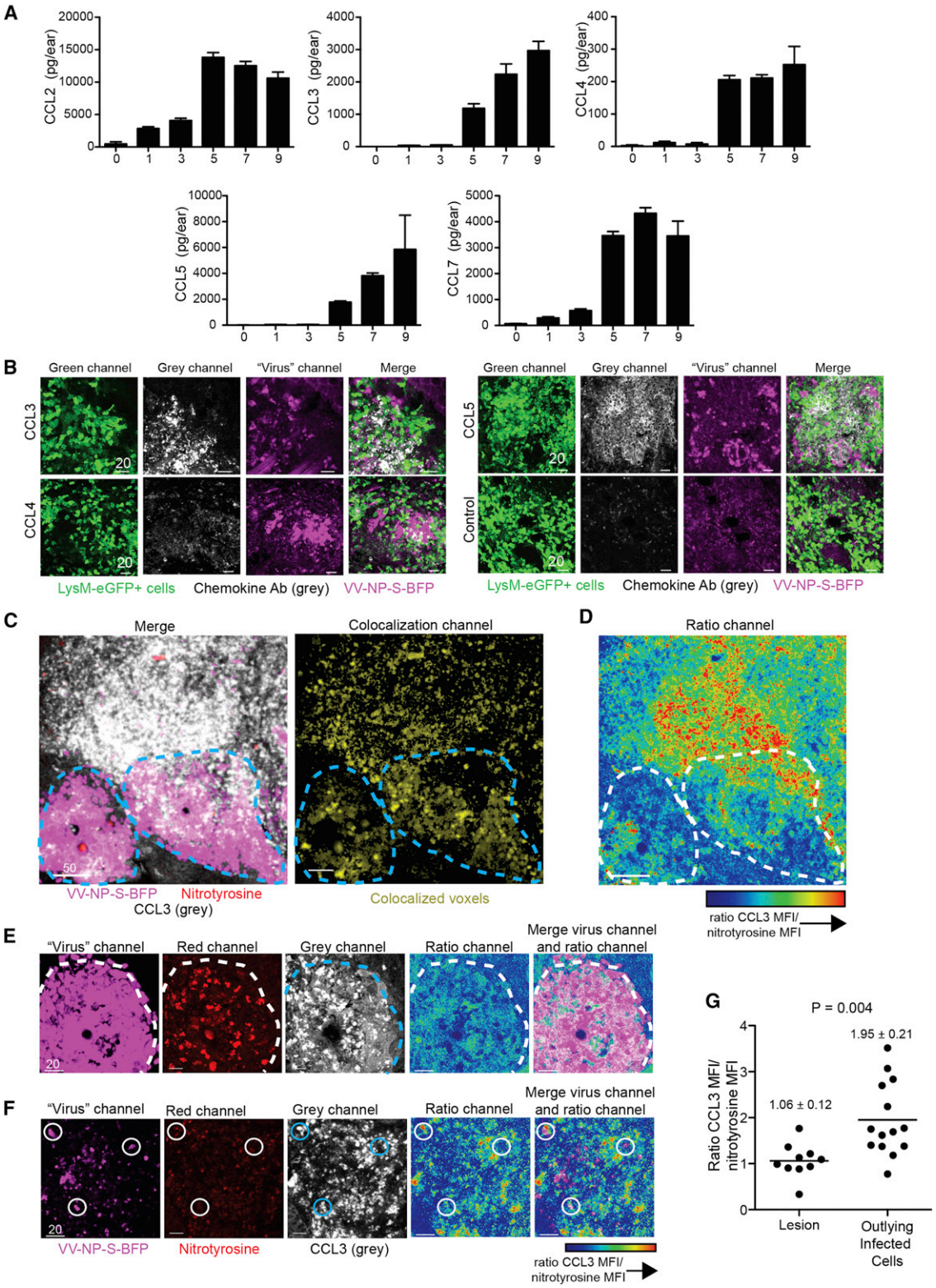

Figure 5. Chemokines Induced by VV Infection Localize to Viral Lesion and Sites of Protein Nitration

(A) Protein levels of chemokines at indicated d.p.i. (x axis) as determined by multiplex protein assay. Scale bar = SEM. Multiplex experiments were performed 3 times with three to six mice per group.

(B) Confocal images of frozen sections from LysM-eGFP mice at 5 d.p.i. with VV-NP-S-BFP (pseudocolored magenta) stained for different chemokines (grey). Antibody chemokine specificity is indicated on left panel. Control = secondary antibody staining alone.

(legend continued on next page)

by codepleting the two cell subsets (Figure 7F). Codepletion increased viral titers >25-fold at 7 d.p.i., far greater an increase than depletion of a single cell type. With continued codepletion, we observed fluorescent lesions (closed, solid) remaining at 14 d.p.i., which we never observed in untreated mice (Figure 7G). Likewise, codepleted ears still contained infectious virus at 14 d.p.i., while controls did not (Figure 7H). Finally, depletion of both cell types resulted in considerable necrosis and pathology in infected ears of antibody-treated mice (Figure 7I).

Taken together, these data lead to the critical conclusion that a spatially coordinated and synergistic attack of innate and adaptive immune effectors is required to control acute viral infection in the skin.

DISCUSSION

While the contributions of the various immune effector cells to controlling a given viral infection are imperfectly known, it is increasingly clear that $CD8^+$ T cells participate in resolving and/or preventing many infections. This has enhanced enthusiasm for vaccines aimed principally at generating protective $CD8^+$ T cell responses (Nolz and Harty, 2011). Fully harnessing the power of $CD8^+$ T cells for vaccines demands knowledge of the optimal method for eliciting cells that provide the most potent antiviral effector function at infection sites. In this study, we used multiphoton microscopy to examine multiple aspects of the $CD8^+$ T cell response to viral infection in situ.

Vaccinia virus robustly replicates in the skin when inoculated via scarification, the current and classical route for smallpox vaccination (Moss, 2001; Yirrell et al., 1994). VV infects both suprabasal epidermal keratinocytes, as expected, but also sizable numbers of mobile inflammatory leukocytes recruited to infected keratinocytic lesions (Figures 1 and 2). Infected inflammatory monocytes produce infectious virus, making them potentially dangerous vehicles for viral dissemination given their high mobility. MPM clearly reveals that $CD8^+$ T cells pursue and eliminate mobile infected cells before they can broadcast virus.

Although the precise kinetics of virus-infected cell killing will require further study, we observed $CD8^+$ T cell lysis of infected inflammatory monocytes minutes after cellular conjugate formation (Movie S3), suggesting that $CD8^+$ T cells are highly efficient at eliminating these cells. Conversely, rather than kill infected keratinocytes, T cells instead patrolled lesion boundaries (Figure 4). A pharmacological blockade of peroxynitrite generation enabled T cells to enter lesions where they could eliminate infected keratinocytes (Figure 6). This demonstrates that T cell entry into lesions is signal limited, likely due to nitration of chemotactic factors in the highly chemically reactive environment generated by $Ly6G^+$ cells infiltrating lesions. This exquisite spatial segregation of $CD8^+$ T cells leads to the surprising conclusion that the majority of Ag-specific antiviral $CD8^+$ T cells in VV-infected ears do not interact with virus-infected cells, even when the latter exists in high numbers. Ergo, simply counting the local $CD8^+$ T cell response is insufficient to gauge the effectiveness of the response since it ignores anatomic complexities that limit $CD8^+$ T cell antiviral activity.

Why would the immune system segregate antiviral effectors? Perhaps this allows $CD8^+$ T cells to focus on mobile infected cells that might escape immune clearance without dallying with infected cells that can be controlled via other means. Alternatively, $CD8^+$ T cells may be dysfunctional or destroyed in the lesion interior in the presence of high levels of ROS/RNS, while monocytes can better handle the chemical stress that they generate themselves.

Although many important questions remain regarding the participation of other innate and adaptive immune cells in resolving peripheral infections and repairing damaged tissues, our findings provide a template for understanding the anatomic specificity of various effector cell functions and underscore the importance of real-time intravital imaging to account for the dynamic behavior of cells as a critical determinant of immunity.

EXPERIMENTAL PROCEDURES

Mice

Specific pathogen-free C57BL/6, B6(Cg)-Tyrc-2J/J (albino B6), and STOCK Tg (CAG-DsRed*MST)1Nagy/J were obtained from The Jackson Laboratory or from Taconic Farms. LysM-eGFP mice (Faust et al., 2000) were acquired through the NIAID Intramural Research Repository and bred in house. STOCK Tg (CAG-DsRed*MST)1Nagy/J were crossed to OT-I TCR transgenic mice (acquired through the NIAID Intramural Research Repository) to create DsRed OT-I mice. In all experiments, 6- to 16-week-old mice were used. All mice were housed under specific pathogen-free conditions (including MNV, MPV, and MHV). All animal procedures were approved by and performed in accordance with the NIAID Animal Care and Use Committee.

Viruses and Infections

Mice were infected epicutaneously in the ear pinna by 10–15 pokes with a bifurcated needle dipped in rVV (stock titer ~1×10^8 pfu/ml). VV-NP-S-eGFP has been previously described (Norbury et al., 2002); VV-NP-S-BFP (with blue fluorescent protein instead of green) was constructed according to established protocols (Earl et al., 2001). VV-BFP-Ub-SIINFEKL was constructed to allow liberation of SIINFEKL peptide by cytosolic ubiquitin hydrolase (described in Fruci et al., 2003).

Adoptive Transfers

$CD8^+$ T cells were purified by negative selection using magnetic-activated cell sorting (MACS) (Miltenyi Biotec). Cells were 90%–95% pure by flow cytometry. A total of 2×10^5 dsRed OT-I cells were transferred prior to infection.

Antibody and Drug Administration

Unless otherwise indicated, mice received 0.5 mg of anti-CD8 (clone 2.43) or GR-1 (clone RB6-8C5), or 0.25 mg of anti-Ly6g (clone 1A8) alone or together

(C) Left panel: Confocal image of a frozen section (WT mouse) at 5 d.p.i. with VV-NP-S-BFP (pseudocolored magenta) stained for nitrotyrosine (red) and CCL3 (grey). Right panel: colocalization of nitrotyrosine and CCL3 staining (yellow). Lesion borders = dashed lines.
(D) Ratiometric image of CCL3 staining/nitrotyrosine staining. Highest ratio of CCL3 to nitrotyrosine is indicated by red coloring as shown in scale bar. Foci borders = dashed lines.
(E) Higher magnification image of a lesion (pseudocolored magenta) at 5 d.p.i. stained for nitrotyrosine (red) and CCL3 (gray). Ratio images (right); lesion borders = dashed lines.
(F) As in (E) but showing region of outlying infected inflammatory monocytes. Infected cell (magenta) surrounded by areas of high CCL3 to nitrotyrosine ratios highlighted by circles.
(G) Numerical calculation of ratio of CCL3 to nitrotyrosine MFI in regions of foci or outlying infected inflammatory monocytes. Mean and SEM are shown. Statistics = Student's t test; scale bars = μm. Confocal imaging experiments were performed twice; N = 6/group.

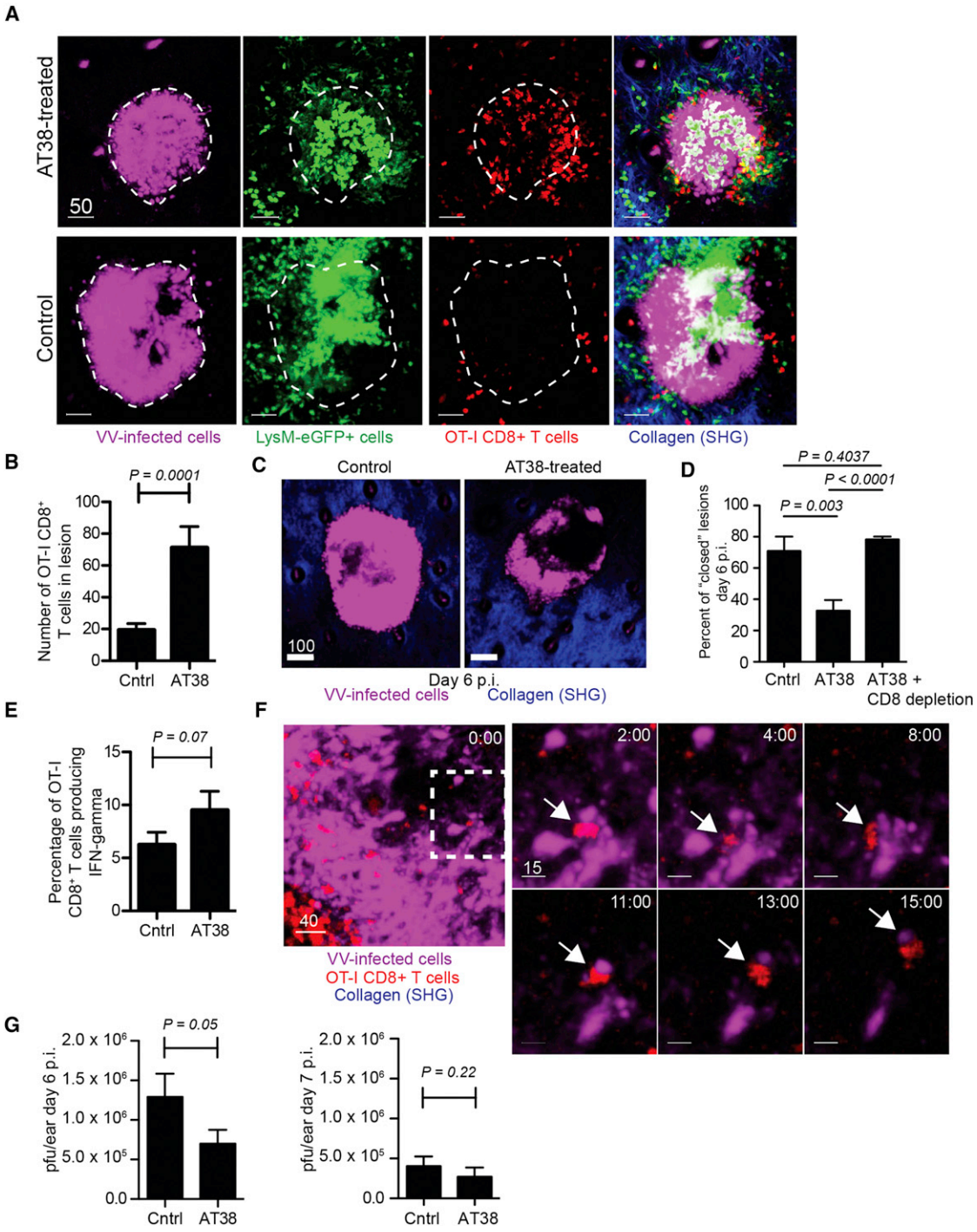

Figure 6. Peroxynitrite Blockade Relocates T Cells into Keratinocytic Lesions

(A) MPM MIP images of LysM-eGFP mice at 5 d.p.i. with VV-NP-S-BFP (magenta). $CD8^+$ T cells (red) were imaged with (top panels) and without (bottom panels) AT38 treatment. Imaging depth was limited to lesion depth (i.e., beneath lesion is not shown).

(B) T cells per lesion ± AT38 as determined by MPM. Results were summed from foci in four mice/group.

(C) MPM images of ears at 6 d.p.i. ± AT38. Foci = magenta, dermis = blue.

(D) Percent of lesions that are closed (e.g., no nonfluorescent center) at 6 d.p.i. ± AT38 determined microscopically. Far column = CD8-depleted, AT38-treated mice.

(E) Percentage of IFN-γ-producing OT-I cells ± AT38 at 6 d.p.i.

(F) MPM image within a VV-NP-S-BFP lesion (magenta) at 5 d.p.i. OT-I $CD8^+$ T cells = red, dashed box = higher magnification (right). Right panels: T cell carrying off a piece of infected keratinocyte. Arrow highlights interaction. Time (min) in upper right.

(G) Viral titers at 6 and 7 d.p.i. ± AT38. Experiments were repeated at least 3 times with three to six mice per group. Error bars = SEM; statistics = Student's t test; scale bars = μm. See also Figure S3 and Movie S4.

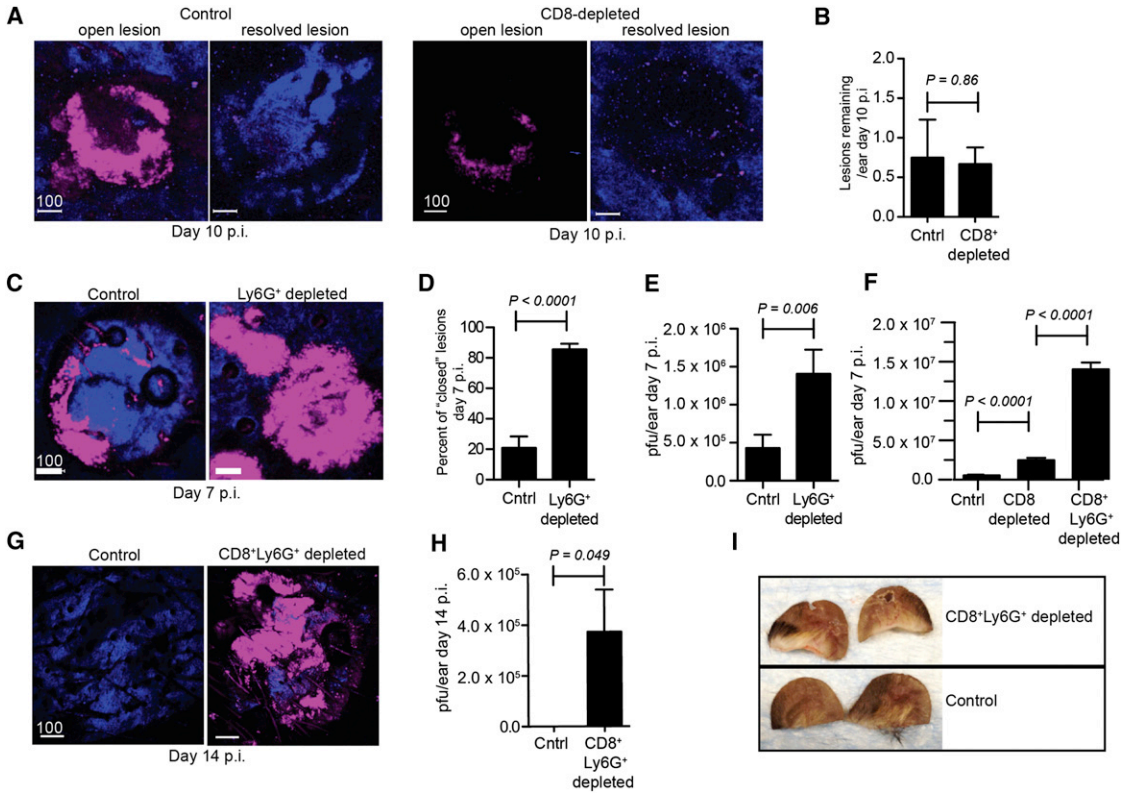

Figure 7. CD8$^+$ T Cells and Ly6G$^+$ Cells Exert Coordinated Control of Peripheral Virus Infection

(A) MPM images at 10 d.p.i. in control (left panels) or CD8-depleted (right panels) mice. Mice were given CD8-antibody beginning on day 6. Lesions = magenta, dermis = blue.

(B) Number of lesions/ear at 10 d.p.i. in control and CD8-depleted mice.

(C) MPM images at 7 d.p.i. ± anti-Ly6G antibody. Lesions = magenta, dermis = blue.

(D and E) Percent of lesions that are closed (e.g., no nonfluorescent center) (D) or viral titers (E) at 7 d.p.i. with Ly6G depletion.

(F) Viral titers at 7 d.p.i. with depletion of CD8 alone (middle) or in conjunction with Ly6G-depletion (right).

(G–I) MPM images (G) at 14 d.p.i., viral titers (H), and photographic images (I) with continuous depletion of CD8$^+$ T and Ly6G$^+$ cells. Experiments (A)–(F) were repeated at least 3 times with three to six mice per group. Experiments (G)–(I) were repeated twice with five mice per group. Scale bar = μm; statistics = Student's t test; error bars = SEM.

intraperitoneally (i.p.) at day 0 and every other day thereafter. For analysis of lesion resolution in the absence of T cells, mice were given anti-CD8 (clone 2.43) on days 6, 8, and 10. Antibodies were purchased from Bio X Cell. AT38 was dissolved in 1% carboxymethylcellulose in sterile saline solution, and 0.5 mg was injected intraperitoneally at 4 or 4 and 5 d.p.i. as indicated.

Flow Cytometric Analyses

Single-cell suspensions of ears were prepared by collagenase digestion (type 2, Worthington Biochemical) and filtration through 70 μm nylon cell strainers. Cells were stained with CD45 (30-F11), CD8 (53-6.7), CD11c (HL3), CD11b (M1/70), CD103 (2E7), Ly6CG (GR-1, RB6-8C5), Ly6G (1A8), F4/80 (BM/8), and CD45.1 (A20) (eBioscience). For staining for IFN-γ production, brefeldin A (10 μg/ml, Sigma-Aldrich) was added during collagenase digestion, and cells were incubated an additional 2 hr in BFA-containing RPMI (Life Technologies). Cells were stained for CD8 and CD45.1, fixed with 3.2% paraformaldehyde, and stained with anti-IFN-γ (clone XMG1.2, eBioscience) in 0.5% saponin. Cells were stained for CellROX (Life Technologies) with a 2 hr incubation.

Viral Titering via Plaque Assay

Ears were collagenase digested, disrupted by pipetting, freeze-thawed 3 times, sonicated 3 times, serially diluted, and plated on TK$^-$ cells. Cells were incubated for 2 days and plaques counted.

Cell Sorting and Plaque Analysis

Ears from five to ten mice per group were dissociated with collagenase, and an aliquot was frozen at this point. Cells were filtered and stained for CD45 (30-F11) and sorted (BD FACSAria) into eGFP$^+$ CD45$^+$ and eGFP$^-$ CD45$^+$ subsets. Sorted cells and the whole-ear aliquot were titered via plaque assay. pfu from sorted cells were normalized to 3 × 10^5 cells, the average number of infected inflammatory monocytes per ear. Percentage contribution of outliers was calculated as pfu per 3 × 10^5 sorted cells/total pfu per ear.

Statistics

Significances were calculated by GraphPad (Prism) using an unpaired Student's t test.

Multiplex Protein Assay

Ears were homogenized in a balanced salt solution supplemented with 0.1% BSA and a complete protease inhibitor cocktail (Roche). Samples were analyzed with a FlowCytomix kit (eBioscience) on a BD LSR II flow cytometer, and values were calculated using FlowCytomix Pro software.

Confocal Microscopy of Frozen Sections

Ears were embedded in OCT medium (Electron Microscopy Sciences) and frozen in dry-ice cooled isopentane. Twenty-micron sections were cut on a Leica cryostat (Leica Microsystems). Sections were fixed in ice-cold acetone for

5 min before blocking with 5% goat or donkey serum then staining with CD8 (53-6.7), CD11b (M1/70), Ly6CG (RB6-8C5), Ly6G (1A8), nitrotyrosine (polyclonal rabbit; Millipore), keratin 5, keratin 6, or keratin 10 (polyclonal rabbit; Abcam). For chemokine staining and nitrotyrosine/chemokine costaining, ears were fixed in PLP fixative overnight, cryoprotected in 15% sucrose, sectioned, and stained with the antibodies CCL3, CCL4, and CCL5 (all goat polyclonal; RND System) followed by detection with donkey anti-goat DyLight 649 and donkey anti-rabbit Rhodamine Red-X (Jackson ImmunoResearch). Sections were incubated with secondary antibodies only as controls, and images were acquired using identical PMT (photomultiplier tube) and laser settings.

Intravital MPM Imaging

MPM imaging was performed as described previously (Hickman et al., 2008). Briefly, images were acquired on an upright Leica SP5 confocal microscope (Leica Microsystems) equipped with two Mai Tai Ti:Sapphire lasers (Spectra-Physics) with 10 watt pumps. Ears were immobilized and bathed in warm saline and imaged with a 20× dipping objective (NA 1.00). Series were obtained in single mode for eGFP/collagen/dsRed imaging (900 nm laser). BFP/collagen/eGFP/dsRed imaging was performed in sequential mode (900 nm and 800 nm lasers). Emitted fluorescence was collected with a four-channel nondescanned detector equipped with a 495 nm dichroic with 460/50 and 525/50 nm bandpass emission filters and a 560 nm dichroic with a 610/60 nm bandpass emission filter. Most movies were acquired using 2× zoom, 3 μm z step (total depth of 45 μm) every 30 s (or 60 s, sequentially). Side-view images were acquired at 1024 × 1024 resolution, 1.5 μm z step, and a total depth of 80–300 μm.

MPM and Confocal Image Analysis

Maximum intensity projections (MIPs) were processed from z stacks using Imaris (Bitplane). Because both collagen (second harmonic generation) and BFP appear in the blue channel, BFP expression was pseudocolored magenta for clarity. In some cases, eGFP was also pseudocolored magenta for continuity in figures. For tracking cellular movement, images were processed using a Gaussian filter, then tracks were calculated using the "spot" function of Imaris. Overlays of tracks were generated using the Imaris XT function "translate tracks" and pseudocolored according to the average speed of the cell creating the track. Average speeds were calculated using the spot detection function and the following parameters: autoregressive motion, gapclose 1, 7.5 μm object diameter, 20 μm maximum distance. Following automated analyses, tracks were analyzed individually for erroneous connections. For analysis of infected cell movement, 2 hr time series were collected, and average cell speed over that time was plotted. Cells were classified as motile outliers if their speed was >4 SDs above speeds for infected keratinocytes. T cells/lesion were calculated manually after using the spot detection function of Imaris to define T cells.

Colocalized voxels of confocal images were calculated using the Imaris Coloc module. Ratiometric images were produced in Fiji ("Math" function) by dividing CCL3 fluorescence intensity by nitrotyrosine fluorescence intensity per voxel. For calculation of CCL3/nitrotyrosine mean fluorescent intensity (MFI), confocal images were collected from areas containing lesions or outlying infected cells with care taken not to mix areas in images. The CCL3 MFI in the entire image was divided by the MFI of the whole image for nitrotyrosine.

SUPPLEMENTAL INFORMATION

Supplemental Information includes three figures and four movies and can be found with this article online at http://dx.doi.org/10.1016/j.chom.2013.01.004.

ACKNOWLEDGMENTS

We thank the Comparative Medicine Branch and staff of the NIH Building 33 vivarium for excellence in animal husbandry. This work was generously supported by the National Institute of Allergy and Infectious Diseases Division of Intramural Research.

Received: July 30, 2012
Revised: November 30, 2012
Accepted: January 9, 2013
Published: February 13, 2013

REFERENCES

Babior, B.M. (2004). NADPH oxidase. Curr. Opin. Immunol. *16*, 42–47.

Bedoui, S., Whitney, P.G., Waithman, J., Eidsmo, L., Wakim, L., Caminschi, I., Allan, R.S., Wojtasiak, M., Shortman, K., Carbone, F.R., et al. (2009). Cross-presentation of viral and self antigens by skin-derived CD103+ dendritic cells. Nat. Immunol. *10*, 488–495.

Chtanova, T., Schaeffer, M., Han, S.J., van Dooren, G.G., Nollmann, M., Herzmark, P., Chan, S.W., Satija, H., Camfield, K., Aaron, H., et al. (2008). Dynamics of neutrophil migration in lymph nodes during infection. Immunity *29*, 487–496.

Deshmane, S.L., Kremlev, S., Amini, S., and Sawaya, B.E. (2009). Monocyte chemoattractant protein-1 (MCP-1): an overview. J. Interferon Cytokine Res. *29*, 313–326.

Earl, P.L., Moss, B., Wyatt, L.S., and Carroll, M.W. (2001). Generation of recombinant vaccinia viruses. Curr. Protoc. Mol. Biol. *Chapter 16*, t16, 17.

Faust, N., Varas, F., Kelly, L.M., Heck, S., and Graf, T. (2000). Insertion of enhanced green fluorescent protein into the lysozyme gene creates mice with green fluorescent granulocytes and macrophages. Blood *96*, 719–726.

Fenner, F., Henderson, D.A., Arita, I., Jezek, Z., and Ladnyi, I. (1988). Smallpox and Its Eradication (Geneva, Switzerland: World Health Organization).

Fischer, M.A., Davies, M.L., Reider, I.E., Heipertz, E.L., Epler, M.R., Sei, J.J., Ingersoll, M.A., Rooijen, N.V., Randolph, G.J., and Norbury, C.C. (2011). $CD11b^+$, $Ly6G^+$ cells produce type I interferon and exhibit tissue protective properties following peripheral virus infection. PLoS Pathog. *7*, e1002374.

Flesch, I.E., Woo, W.P., Wang, Y., Panchanathan, V., Wong, Y.C., La Gruta, N.L., Cukalac, T., and Tscharke, D.C. (2010). Altered CD8(+) T cell immunodominance after vaccinia virus infection and the naive repertoire in inbred and F(1) mice. J. Immunol. *184*, 45–55.

Freedberg, I.M., Tomic-Canic, M., Komine, M., and Blumenberg, M. (2001). Keratins and the keratinocyte activation cycle. J. Invest. Dermatol. *116*, 633–640.

Fruci, D., Lauvau, G., Saveanu, L., Amicosante, M., Butler, R.H., Polack, A., Ginhoux, F., Lemonnier, F., Firat, H., and van Endert, P.M. (2003). Quantifying recruitment of cytosolic peptides for HLA class I presentation: impact of TAP transport. J. Immunol. *170*, 2977–2984.

Halliwell, B. (2006). Phagocyte-derived reactive species: salvation or suicide? Trends Biochem. Sci. *31*, 509–515.

Hersperger, A.R., Siciliano, N.A., and Eisenlohr, L.C. (2012). Comparable polyfunctionality of ectromelia virus- and vaccinia virus-specific murine T cells despite markedly different in vivo replication and pathogenicity. J. Virol. *86*, 7298–7309.

Hickman, H.D., Takeda, K., Skon, C.N., Murray, F.R., Hensley, S.E., Loomis, J., Barber, G.N., Bennink, J.R., and Yewdell, J.W. (2008). Direct priming of antiviral CD8+ T cells in the peripheral interfollicular region of lymph nodes. Nat. Immunol. *9*, 155–165.

Hickman, H.D., Li, L., Reynoso, G.V., Rubin, E.J., Skon, C.N., Mays, J.W., Gibbs, J., Schwartz, O., Bennink, J.R., and Yewdell, J.W. (2011). Chemokines control naive CD8+ T cell selection of optimal lymph node antigen presenting cells. J. Exp. Med. *208*, 2511–2524.

Iannacone, M., Moseman, E.A., Tonti, E., Bosurgi, L., Junt, T., Henrickson, S.E., Whelan, S.P., Guidotti, L.G., and von Andrian, U.H. (2010). Subcapsular sinus macrophages prevent CNS invasion on peripheral infection with a neurotropic virus. Nature *465*, 1079–1083.

Jiang, X., Clark, R.A., Liu, L., Wagers, A.J., Fuhlbrigge, R.C., and Kupper, T.S. (2012). Skin infection generates non-migratory memory CD8+ T(RM) cells providing global skin immunity. Nature *483*, 227–231.

Junt, T., Moseman, E.A., Iannacone, M., Massberg, S., Lang, P.A., Boes, M., Fink, K., Henrickson, S.E., Shayakhmetov, D.M., Di Paolo, N.C., et al. (2007). Subcapsular sinus macrophages in lymph nodes clear lymph-borne viruses and present them to antiviral B cells. Nature *450*, 110–114.

Lane, H.C., Montagne, J.L., and Fauci, A.S. (2001). Bioterrorism: a clear and present danger. Nat. Med. *7*, 1271–1273.

Lev, A., Princiotta, M.F., Zanker, D., Takeda, K., Gibbs, J.S., Kumagai, C., Waffarn, E., Dolan, B.P., Burgevin, A., Van Endert, P., et al. (2010). Compartmentalized MHC class I antigen processing enhances immunosurveillance by circumventing the law of mass action. Proc. Natl. Acad. Sci. USA *107*, 6964–6969.

Li, J.L., Goh, C.C., Keeble, J.L., Qin, J.S., Roediger, B., Jain, R., Wang, Y., Chew, W.K., Weninger, W., and Ng, L.G. (2012). Intravital multiphoton imaging of immune responses in the mouse ear skin. Nat. Protoc. *7*, 221–234.

Lindquist, R.L., Shakhar, G., Dudziak, D., Wardemann, H., Eisenreich, T., Dustin, M.L., and Nussenzweig, M.C. (2004). Visualizing dendritic cell networks in vivo. Nat. Immunol. *5*, 1243–1250.

Liu, L., Zhong, Q., Tian, T., Dubin, K., Athale, S.K., and Kupper, T.S. (2010). Epidermal injury and infection during poxvirus immunization is crucial for the generation of highly protective T cell-mediated immunity. Nat. Med. *16*, 224–227.

Molon, B., Ugel, S., Del Pozzo, F., Soldani, C., Zilio, S., Avella, D., De Palma, A., Mauri, P., Monegal, A., Rescigno, M., et al. (2011). Chemokine nitration prevents intratumoral infiltration of antigen-specific T cells. J. Exp. Med. *208*, 1949–1962.

Moss, B. (2001). Poxviridae: the viruses and their replication. In Fields Virology, fourth edition, D.M. Knipe and P.M. Howley, eds. (Philadelphia: Lippincott, Williams, and Wilkins), pp. 2849–2884.

Moutaftsi, M., Peters, B., Pasquetto, V., Tscharke, D.C., Sidney, J., Bui, H.H., Grey, H., and Sette, A. (2006). A consensus epitope prediction approach identifies the breadth of murine T(CD8+)-cell responses to vaccinia virus. Nat. Biotechnol. *24*, 817–819.

Moutaftsi, M., Salek-Ardakani, S., Croft, M., Peters, B., Sidney, J., Grey, H., and Sette, A. (2009). Correlates of protection efficacy induced by vaccinia virus-specific CD8+ T-cell epitopes in the murine intranasal challenge model. Eur. J. Immunol. *39*, 717–722.

Navarro, J.M., Casatorres, J., and Jorcano, J.L. (1995). Elements controlling the expression and induction of the skin hyperproliferation-associated keratin K6. J. Biol. Chem. *270*, 21362–21367.

Nolz, J.C., and Harty, J.T. (2011). Strategies and implications for prime-boost vaccination to generate memory CD8 T cells. Adv. Exp. Med. Biol. *780*, 69–83.

Norbury, C.C., Malide, D., Gibbs, J.S., Bennink, J.R., and Yewdell, J.W. (2002). Visualizing priming of virus-specific CD8+ T cells by infected dendritic cells in vivo. Nat. Immunol. *3*, 265–271.

Remakus, S., and Sigal, L.J. (2011). Gamma interferon and perforin control the strength, but not the hierarchy, of immunodominance of an antiviral CD8+ T cell response. J. Virol. *85*, 12578–12584.

Salek-Ardakani, S., Arens, R., Flynn, R., Sette, A., Schoenberger, S.P., and Croft, M. (2009). Preferential use of B7.2 and not B7.1 in priming of vaccinia virus-specific CD8 T cells. J. Immunol. *182*, 2909–2918.

Seedhom, M.O., Mathurin, K.S., Kim, S.K., and Welsh, R.M. (2012). Increased protection from vaccinia virus infection in mice genetically prone to lymphoproliferative disorders. J. Virol. *86*, 6010–6022.

Simon, I.D., Publicover, J., and Rose, J.K. (2007). Replication and propagation of attenuated vesicular stomatitis virus vectors in vivo: vector spread correlates with induction of immune responses and persistence of genomic RNA. J. Virol. *81*, 2078–2082.

Sutter, G., and Moss, B. (1992). Nonreplicating vaccinia vector efficiently expresses recombinant genes. Proc. Natl. Acad. Sci. USA *89*, 10847–10851.

Szabó, C., Ischiropoulos, H., and Radi, R. (2007). Peroxynitrite: biochemistry, pathophysiology and development of therapeutics. Nat. Rev. Drug Discov. *6*, 662–680.

Tscharke, D.C., Karupiah, G., Zhou, J., Palmore, T., Irvine, K.R., Haeryfar, S.M., Williams, S., Sidney, J., Sette, A., Bennink, J.R., and Yewdell, J.W. (2005). Identification of poxvirus CD8+ T cell determinants to enable rational design and characterization of smallpox vaccines. J. Exp. Med. *201*, 95–104.

Tscharke, D.C., Woo, W.P., Sakala, I.G., Sidney, J., Sette, A., Moss, D.J., Bennink, J.R., Karupiah, G., and Yewdell, J.W. (2006). Poxvirus CD8+ T-cell determinants and cross-reactivity in BALB/c mice. J. Virol. *80*, 6318–6323.

Weiss, R.A., Eichner, R., and Sun, T.T. (1984). Monoclonal antibody analysis of keratin expression in epidermal diseases: a 48- and 56-kdalton keratin as molecular markers for hyperproliferative keratinocytes. J. Cell Biol. *98*, 1397–1406.

Werner, S., and Grose, R. (2003). Regulation of wound healing by growth factors and cytokines. Physiol. Rev. *83*, 835–870.

Xu, R., Johnson, A.J., Liggitt, D., and Bevan, M.J. (2004). Cellular and humoral immunity against vaccinia virus infection of mice. J. Immunol. *172*, 6265–6271.

Yewdell, J.W. (2006). Confronting complexity: real-world immunodominance in antiviral CD8+ T cell responses. Immunity *25*, 533–543.

Yirrell, D.L., Norval, M., and Reid, H.W. (1994). Local epidermal viral infections: comparative aspects of vaccinia virus, herpes simplex virus and human papillomavirus in man and orf virus in sheep. FEMS Immunol. Med. Microbiol. *8*, 1–12.

Zhao, Y., and Croft, M. (2012). Dispensable role for 4-1BB and 4-1BBL in development of vaccinia virus-specific CD8 T cells. Immunol. Lett. *141*, 220–226.